CMS Physics Analysis Summary

Contact: cms-pag-conveners-bphysics@cern.ch 2013/04/09

Angular analysis and branching ratio measurement of the decay $B^0 \to K^{*0}\mu^+\mu^-$

The CMS Collaboration

Abstract

The angular distributions and the differential branching fraction of the decay $B^0 \to K^{*0}\mu^+\mu^-$ are studied using an integrated luminosity of 5.2 fb^{-1} of data collected with the CMS detector. The forward-backward asymmetry of the muons A_{FB}, the K^{*0} longitudinal polarization fraction F_L, and the differential branching fraction $d\mathcal{B}/dq^2$, are determined as a function of the dimuon invariant mass squared. The measurements are in good agreement with the standard model.

1 Introduction

New phenomena, beyond the standard model (SM) of particle physics, may be observed directly or through their influence on other physics processes. Indirect searches for new phenomena generally proceed by comparing experimental and theoretical results in the production or decay of known particles. Good candidates for these types of searches generally satisfy four criteria: small SM rates, small theoretical uncertainties, new physics predictions that differ from the SM, and experimental accessibility. One productive area which meets these criteria is the study of flavor-changing neutral current decays of b hadrons such as the semileptonic decay mode $B^0 \to K^{*0}\mu^+\mu^-$ (charge conjugate states are implied unless explicitly stated otherwise). This decay is forbidden at tree level in the SM, resulting in small SM rates. From a theoretical side, robust calculations are now possible for much of the phase space of this decay and the calculations also indicate that new physics could give rise to readily observable effects. Finally, this decay mode is relatively easy to select and reconstruct at hadron colliders.

Two important observables in the $B^0 \to K^{*0}\mu^+\mu^-$ decay are the forward-backward asymmetry of the muons, A_{FB}, and the longitudinal polarization fraction of the $K^*(892)$, F_L. These can be measured as a function of the q^2 of the decay (dimuon invariant mass squared) and compared to SM predictions [1–3]. Deviations from the SM predictions may indicate new phenomena. While previous measurements by BaBar, Belle, CDF, and LHCb are consistent with the standard model [4–7], these measurements are still statistics limited and new results may provide an indication of new physics.

This paper presents measurements of A_{FB}, F_L, and the differential branching fraction $d\mathcal{B}/dq^2$ from $B^0 \to K^{*0}\mu^+\mu^-$ decays, using data collected from pp collisions at the Compact Muon Solenoid (CMS) experiment in 2011 at a center of mass energy of 7 TeV. The amount of analyzed data corresponds to an integrated luminosity of $5.2\pm0.1\,\text{fb}^{-1}$ [8]. The K^{*0} is reconstructed through its decay into the $K^+\pi^-$ final state and the B^0 is reconstructed by fitting the two identified muon tracks and the two hadron tracks to a common vertex. The values of A_{FB} and F_L are measured by fitting the event distribution as a function of two angular variables, the angle between the positive charged muon and the B^0 in the dimuon rest frame, and the angle between the kaon and the B^0 in the K^{*0} rest frame. All measurements are performed in q^2 bins from 1 to 19 $(\text{GeV}/c^2)^2$. The q^2 bins $8.68 < q^2 < 10.09\,(\text{GeV}/c^2)^2$ and $12.9 < q^2 < 14.18\,(\text{GeV}/c^2)^2$, corresponding to the $B^0 \to K^{*0}J/\psi$ and $B^0 \to K^{*0}\psi'$ decays, respectively, are used to validate the analysis and as normalization for the branching fraction measurement.

2 Detector

A detailed description of the CMS detector may be found elsewhere [9]. The main detector components used in this analysis are the silicon tracker and the muon detection systems. The silicon tracker measures charged particles within the pseudorapidity range $|\eta| < 2.5$, where $\eta = -\ln[\tan(\theta/2)]$ and θ is the polar angle of the track relative to the counterclockwise beam direction. It consists of 1440 silicon pixel and 15148 silicon strip detector modules and is located in the 3.8 T field of the superconducting solenoid. It provides an impact parameter resolution of about 15 μm and a p_T resolution of about 1.5% for particles with transverse momenta up to 100 GeV/c. Muons are measured in the pseudorapidity range $|\eta| < 2.4$, with detection planes made using three technologies: drift tubes, cathode strip chambers, and resistive plate chambers. Events are recorded with a two-level trigger system. The first level is composed of custom hardware processors and uses information from the calorimeters and muon systems to select the most interesting events. The high-level trigger processor farm further decreases the event

rate from nearly 100 kHz to around 350 Hz before data storage.

3 Reconstruction, Event Selection, and Efficiency

The signal ($B^0 \to K^{*0}\mu^+\mu^-$) and normalization/control samples ($B^0 \to K^{*0}J/\psi$ and $B^0 \to K^{*0}\psi'$) were recorded with the same trigger, requiring two identified muons to form a vertex that is displaced from the pp collision region (beamspot). Five triggers were used during 2011 with increasingly stringent requirements to maintain an acceptable trigger rate as the instantaneous luminosity increased. For all triggers, the separation between the beamspot and the dimuon vertex in the transverse plane was required to be larger than three times the quadratic sum of the distance uncertainty and the beamspot size. In addition, the cosine of angle between the dimuon momentum vector and the vector between the beamspot and the dimuon vertex in the transverse plane was required to be greater than 0.9. More than 95% of the data were collected with triggers that required muon pseudorapidity of $|\eta(\mu)| < 2.2$, dimuon transverse momentum of $p_T(\mu\mu) > 6.9\,\text{GeV}/c$, single muon transverse momentum for both muons of $p_T(\mu) > 3, 4, 4.5, 5\,\text{GeV}/c$ (depending on trigger), and dimuon vertex fit probability of $\chi^2_{\text{prob}} > 5\%, 15\%$ (depending on trigger). The remaining 5% of the data were obtained from a trigger with somewhat looser selection criteria. The events used in this analysis passed at least one of the five triggers.

The decay modes used in this analysis require two muon candidates and two hadron candidates, obtained from offline reconstruction. The muon candidates are required to match the muons that caused the trigger and to pass several muon identification requirements: match of track with at least one muon segment, track fit χ^2 per degree of freedom less than 1.8, at least 11 hits in the tracker, with at least 2 from the pixel detector, and a transverse (longitudinal) impact parameter less than 3 cm (30 cm). The offline muons must also pass the same requirements used in the trigger. In events where multiple triggers are passed, the requirements associated with the loosest trigger are used.

While the muon requirements are based on the trigger and a standard selection, most of the remaining selection criteria were optimized by maximizing $S/\sqrt{S+B}$ where S is the expected signal from Monte Carlo simulations and B is the background estimated from data sidebands more than $3\sigma_{m(B^0)}$ and less than $5.5\sigma_{m(B^0)}$ from the B^0 mass, where $\sigma_{m(B^0)}$ is the average B^0 mass resolution. The optimization was performed on one trigger sample, corresponding to $2.7\,\text{fb}^{-1}$, and only in the region far from the J/ψ and ψ' peaks: $1 < q^2 < 7.3$ and $16 < q^2 < 19\,(\text{GeV}/c^2)^2$. The hadron track candidates must fail the muon identification criteria, have $p_T(h) > 0.75\,\text{GeV}/c$, and have an extrapolated distance of closest approach to the beamspot in the transverse plane greater than 1.3 times the quadratic sum of the distance uncertainty and the beamspot transverse size. The two hadron candidates must have an invariant mass within $80\,\text{MeV}/c^2$ of the nominal K^{*0} mass for either the $K^+\pi^-$ or $K^-\pi^+$ hypothesis. To remove contamination from ϕ decays, the hadron pair invariant mass must be greater than $1.035\,\text{GeV}/c^2$ when the K^+ rest mass is assigned to both hadron tracks. The B^0 candidates are obtained by fitting the four charged tracks to a common vertex and applying a vertex constraint to improve the track parameters. The B^0 candidates must have $p_T(B^0) > 8\,\text{GeV}/c$, $|\eta(B^0)| < 2.2$, vertex fit $\chi^2_{\text{prob}} > 9\%$, vertex transverse separation from the beamspot greater than 12 times the quadratic sum of the separation uncertainty and the beamspot transverse size, and $\cos\alpha^{B^0}_{xy} > 0.9994$ where $\alpha^{B^0}_{xy}$ is the angle, in the transverse plane, between the B^0 momentum vector and the line-of-flight between the beamspot and the B^0 vertex. The invariant mass of the four-track vertex must also be within $280\,\text{MeV}/c^2$ of the nominal B^0 mass for either the $K^-\pi^+\mu^+\mu^-$ or

$K^+\pi^-\mu^+\mu^-$ hypothesis. This selection results in an average of 1.06 candidates per event in which at least one candidate is found. A single candidate is chosen from each event based on the best B^0 vertex fit χ^2.

The four-track vertex candidate is identified as a B^0 $\left(\overline{B}^0\right)$ if the $K^+\pi^-$ $\left(K^-\pi^+\right)$ is closest to the nominal K^{*0} mass. In cases where both $K\pi$ combinations are within 50 MeV/c^2 of the nominal K^{*0} mass, no clear identification is possible as the natural width of the K^{*0} is approximately 50 MeV/c^2, and therefore the event is rejected. The fraction of events assigned the incorrect state is estimated from simulations to be 8%.

From the retained events, the dimuon invariant mass $m(\mu\mu)$ and its corresponding calculated uncertainty $\sigma_{m(\mu\mu)}$ are used to distinguish between the signal and normalization/control samples. The $B^0 \to K^{*0}J/\psi$ and $B^0 \to K^{*0}\psi'$ samples are defined as $m_{J/\psi} - 5\sigma_{m(\mu\mu)} < m(\mu\mu) < m_{J/\psi} + 3\sigma_{m(\mu\mu)}$ and $|m(\mu\mu) - m_{\psi'}| < 3\sigma_{m(\mu\mu)}$, respectively. The asymmetric selection of the J/ψ sample is due to the radiative tail in the dimuon spectrum while the smaller signal in the ψ' mode made an asymmetric cut unnecessary. The signal sample is the complement of the J/ψ and ψ' samples.

The global efficiency ϵ is the product of the acceptance and the reconstruction and selection efficiency, both of which are obtained from Monte Carlo simulations (MC). The pp collision is simulated using PYTHIA [10], the unstable particles are decayed by EVTGEN [11], and the particles are traced through a detailed model of the detector with GEANT4 [12]. The reconstruction and event selection proceeds as for the data events. Three simulation samples were created in which the B^0 was forced to decay to either $B^0 \to K^{*0}(K^+\pi^-)\mu^+\mu^-$, $B^0 \to K^{*0}(K^+\pi^-)J/\psi(\mu^+\mu^-)$, or $B^0 \to K^{*0}(K^+\pi^-)\psi'(\mu^+\mu^-)$. The acceptance is calculated as the fraction of events passing the single muon cuts of $p_T(\mu) > 2.8\,\text{GeV}/c$ and $|\eta(\mu)| < 2.3$ relative to all events with a B^0 in the event with $p_T(B^0) > 8\,\text{GeV}/c$ and $|\eta(B^0)| < 2.2$. The acceptance is obtained from the generated events up through the EVTGEN step. To obtain the reconstruction and selection efficiency, the Monte Carlo events were divided into five parts, appropriately sized to match the amount of data taken with each of the five trigger versions. In each of the five samples, the appropriate trigger and matching offline event selection was applied. Furthermore, each of the five samples was reweighted to obtain the correct distribution of pileup events (pp collisions in addition to the source of the dimuons), corresponding to the data period during which the trigger was active. The reconstruction and selection efficiency is the fraction of events which pass all cuts and have a reconstructed B^0 compatible with the generated B^0 in the event relative to the events which pass the acceptance criteria.

4 Analysis

The analysis is designed to measure the forward-backward asymmetry of the muons, A_{FB}, the $K^*(892)$ longitudinal polarization fraction, F_L, and the differential branching fraction, $d\mathcal{B}/dq^2$, of the decay $B^0 \to K^{*0}\mu^+\mu^-$ as a function of the dimuon invariant mass squared (q^2).

Figure 1 defines the relevant angular observables and Eq. 1 describes the dependence of the decay-rate as a function of these variables. The angle θ_K is defined as the angle between the kaon momentum and the direction opposite to the B^0 $\left(\overline{B}^0\right)$ in the K^{*0} $\left(\overline{K}^{*0}\right)$ rest frame, while the angle θ_l is defined as the angle between the positive (negative) muon momentum and the direction opposite to the B^0 $\left(\overline{B}^0\right)$ in the dimuon reference frame. Although the $K^+\pi^-$ invariant mass must be consistent with a K^{*0}, there can be contributions from a spinless (S-wave) $K^+\pi^-$ combination. The S-wave fraction is described by F_S while the interference between the S-wave and P-wave decays is determined by A_S.

$$\begin{aligned}\frac{1}{\Gamma}\frac{\mathrm{d}^3\Gamma}{\mathrm{d}\cos\theta_K \mathrm{d}\cos\theta_l \mathrm{d}q^2} = \frac{9}{16}\Bigg\{ &\left[\frac{2}{3}F_S + \frac{4}{3}A_S\cos\theta_K\right]\left(1-\cos^2\theta_l\right) \\ &+ \left(1-F_S\right)\Big[2F_L\cos^2\theta_K\left(1-\cos^2\theta_l\right) \\ &+ \frac{1}{2}\left(1-F_L\right)\left(1-\cos^2\theta_K\right)\left(1+\cos^2\theta_l\right) \\ &+ \frac{4}{3}A_{FB}\left(1-\cos^2\theta_K\right)\cos\theta_l\Big]\Bigg\}.\end{aligned} \tag{1}$$

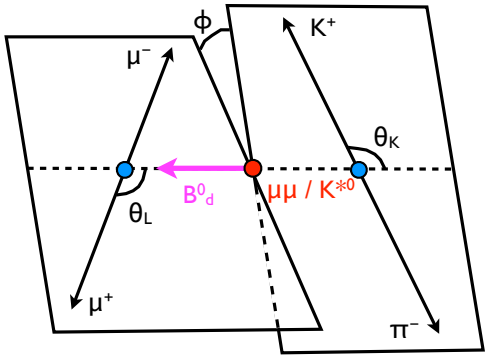

Figure 1: Sketch showing the definition of the angular observables for the decay $\mathrm{B}^0 \to \mathrm{K}^{*0}\mu^+\mu^-$.

The main results of the analysis are extracted from unbinned extended maximum likelihood fits to three variables: the B^0 invariant mass and the two angular variables θ_K and θ_l. For each q^2 bin, the p.d.f. has the following mathematical expression:

$$\begin{aligned}\text{p.d.f.}(m,\cos\theta_K,\cos\theta_l) = &\; Y_S\; S(m)\cdot S(\cos\theta_K,\cos\theta_l)\cdot\epsilon(\cos\theta_K,\cos\theta_l) \\ &+ Y_B^c\; B^c(m)\cdot B^c(\cos\theta_K)\cdot B^c(\cos\theta_l) \\ &+ Y_B^p\; B^p(m)\cdot B^p(\cos\theta_K)\cdot B^p(\cos\theta_l).\end{aligned} \tag{2}$$

The signal yield is given by the free parameter Y_S and the signal shape is described by the function $S(m)$ in the invariant mass variable and the product of the theoretical signal shape in the two angular variables, $S(\cos\theta_K,\cos\theta_l)$, and the efficiency in the two angular variables, $\epsilon(\cos\theta_K,\cos\theta_l)$. The signal mass shape $S(m)$ is a double Gaussian with a common mean. While the mean is free to float, the two resolution parameters and the relative fraction are fixed to the result from a fit to the simulated events. The signal angular function $S(\cos\theta_K,\cos\theta_l)$ is given by Eq. 1. The efficiency function $\epsilon(\cos\theta_K,\cos\theta_l)$ is a polynomial in $\cos\theta_l$ and $\cos\theta_K$ and is obtained by fitting two-dimensional efficiency histograms (6 $\cos\theta_K$ bins and 5 $\cos\theta_l$ bins). The $\cos\theta_K$ polynomial is degree 3 while the $\cos\theta_l$ polynomial is degree 6 (with 1st and 5th orders removed). For some q^2 bins, simpler polynomials are used as they are sufficient to describe the data. There are two contributions to the background, with yields given by Y_B^p for the "peaking" background and Y_B^c for the "combinatorial" background. The peaking background is due to the remaining $\mathrm{B}^0 \to \mathrm{K}^{*0}\mathrm{J}/\psi$ and $\mathrm{B}^0 \to \mathrm{K}^{*0}\psi'$ decays, not removed by the normalized dimuon mass cut or the q^2 cut. For these events, the dimuon mass is reconstructed far from the true mass, which results in a reconstructed B^0 mass similarly displaced from the true B^0 mass. The shapes of this background in the mass, $B^p(m)$, and angular variables, $B^p(\cos\theta_K)$ and $B^p(\cos\theta_l)$, are obtained from simulation of $\mathrm{B}^0 \to \mathrm{K}^{*0}\mathrm{J}/\psi$ and $\mathrm{B}^0 \to \mathrm{K}^{*0}\psi'$ events, fit to double Gaussians

in mass and polynomials in $\cos\theta_K$ and $\cos\theta_l$. The background yield is also obtained from simulation, properly normalized by comparing the reconstructed $\mathrm{B}^0 \to \mathrm{K}^{*0}\mathrm{J}/\psi$ and $\mathrm{B}^0 \to \mathrm{K}^{*0}\psi'$ yields in data and MC. The remaining background, combinatorial in nature, is described by a single exponential in mass, $B^c(m)$, and a polynomial, varying between degree 0 and 4 as needed to describe the data, in each angular variable, $B^c(\cos\theta_K)$ and $B^c(\cos\theta_l)$.

The important results of the fit, in each q^2 bin (including the J/ψ and ψ' bins), are the muon forward-backward asymmetry A_{FB} and the K^{*0} longitudinal polarization fraction F_L. In the fits to the data, the parameters that define the shapes of $S(m)$, $B^p(m)$, $B^p(\cos\theta_K)$, and $B^p(\cos\theta_l)$ (except the mass parameter in $S(m)$), as well as the yield Y_B^p, are initially set to the values obtained from simulation, with a Gaussian constraint defined by the uncertainty found in the fit to the simulated events. The first fit to the data is to the normalization samples ($\mathrm{B}^0 \to \mathrm{K}^{*0}\mathrm{J}/\psi$ and $\mathrm{B}^0 \to \mathrm{K}^{*0}\psi'$). The values for F_S and A_S from the fit to $\mathrm{B}^0 \to \mathrm{K}^{*0}\mathrm{J}/\psi$ fit are used in the signal q^2 bins, with Gaussian constraints defined by the uncertainty from the fit. The longitudinal polarization fraction F_L and the scalar fraction F_S are constrained to lie in the physical region of 0 to 1. In addition, penalty terms are added to ensure that $|A_{FB}| < \frac{3}{4}(1 - F_L)$ and $|A_S| < \frac{1}{2}(F_s + 3F_L(1 - F_S))$, which are necessary to have a non-negative decay rate.

The differential branching fraction, $\mathrm{d}\mathcal{B}/\mathrm{d}q^2$, is measured relative to the normalization channel $\mathrm{B}^0 \to \mathrm{K}^{*0}\mathrm{J}/\psi$ and multiplied by the known branching fraction for this channel:

$$\frac{\mathrm{d}\mathcal{B}\left(\mathrm{B}^0 \to \mathrm{K}^{*0}\mu^+\mu^-\right)}{\mathrm{d}q^2} = \frac{Y_S}{Y_N}\frac{\epsilon_N}{\epsilon_S}\frac{\mathcal{B}\left(\mathrm{B}^0 \to \mathrm{K}^{*0}\mathrm{J}/\psi\right)}{\mathrm{d}q^2}, \tag{3}$$

where Y_S, Y_N are the yields of the signal and normalization channels, respectively, ϵ_S, ϵ_N are the efficiencies of the signal and normalization channels, respectively, and $\mathcal{B}\left(\mathrm{B}^0 \to \mathrm{K}^{*0}\mathrm{J}/\psi\right)$ is the world average branching fraction for the normalization channel [13]. The yields are obtained by fits to the invariant mass distributions and the efficiencies are obtained by integrating over the angular variables using the values obtained from the previously described fits.

Several methods were used to validate the fit formalism and results. First, toy MC samples were used to check for bias and verify the correctness of the estimated statistical uncertainties. Second, a fit was performed to a sample of MC events that approximated the true data sample. In addition to correctly normalized samples of simulated $\mathrm{B}^0 \to \mathrm{K}^{*0}\mu^+\mu^-$, $\mathrm{B}^0 \to \mathrm{K}^{*0}\mathrm{J}/\psi$, and $\mathrm{B}^0 \to \mathrm{K}^{*0}\psi'$ events, combinatorial background events were added based on the assumed distributions from the p.d.f. Finally, the fit was performed on the normalization/control samples and the results compared to the known values. Discrepancies from these checks with expectations were treated as systematic uncertainties, as described in Sec. 5.

5 Systematic Uncertainties

A variety of systematic effects were investigated and the impact on the measurements of F_L, A_{FB}, and $\mathrm{d}\mathcal{B}/\mathrm{d}q^2$ evaluated. The finite size of the MC samples used to measure the efficiency introduce a systematic uncertainty of a statistical nature. A set of alternative efficiency functions were created by randomly varying the parameters of the efficiency polynomials within the fitted uncertainties on the MC samples. The alternative efficiency functions were applied to the data and the root-mean-squares of the returned values were taken as the systematic uncertainty. The systematic uncertainty from toy MC studies is obtained from the observed bias when 1000 pseudo-experiments are generated and fit with the p.d.f. of Eq. 2. The full MC validation systematic uncertainty is obtained from biases found from a fit (using the p.d.f. of Eq. 2) to a MC sample similar to the analyzed data set. Mistagging of a B^0 as a $\overline{\mathrm{B}}^0$ (and vice

versa) increases the measured B^0 resolution. A comparison of resolutions for data and MC (varying the mistag rates in MC) indicates the mistag rate may be as high as 12%, compared to the MC default value of 8%. The systematic uncertainty on the mistag uncertainty is obtained from the difference in results from these two values. The systematic uncertainty related to the contribution from $K\pi$ S-wave (and interference with the $P-$wave) is evaluated by taking the difference between the default results, obtained by fitting with a function accounting for the S-wave, with the results from a fit performed with no S-wave or interference terms. Variations of the background p.d.f. shapes, versus mass and angles, were used to estimate the effect from non-optimal p.d.f. shapes. The double-Gaussian shape parameters of the peaking background, normally taken from a fit to the simulation, were left free in the data fit and the difference taken as a systematic uncertainty. The degree of the polynomials used to fit the angular shapes of the combinatorial background were increased by 1 and the difference taken as a systematic uncertainty. The signal mass shape uncertainty was evaluated by allowing the signal mass shape parameters to be fit from the data, rather than from simulations. Reasonable variation of the number of simultaneous pp collisions in an event (pileup) was found to have no effect on the efficiency. The effect of the experimental resolution of $\cos\theta_K$ and $\cos\theta_l$ was estimated as the difference, when significant, in A_{FB} and F_L when the reconstructed or generated values of $\cos\theta_K$ and $\cos\theta_l$ were used. The effect of the dimuon mass resolution was found to be negligible on the final results. For the differential branching fraction measurement, there is an additional systematic uncertainty associated with the check of the $B^0 \to K^{*0}J/\psi$ to $B^0 \to K^{*0}\psi'$ branching ratio. While the measured value of 15.5 ± 0.4 (statistical uncertainty only) is in agreement with the world average value of 16.8 ± 2.4 [13], a systematic uncertainty equal to the relative uncertainty of the average value (14.3%) was assigned due to the limited power of the test. The systematic uncertainties are measured and applied in each q^2 bin. A summary of the systematic uncertainties is given in Table 1; the ranges give the variation over the q^2 bins.

Table 1: Uncorrelated systematic uncertainty contributions for the measurements of F_L, A_{FB}, and $d\mathcal{B}/dq^2$.

Systematic uncertainty	F_L	A_{FB}	$d\mathcal{B}/dq^2$
Efficiency statistical uncertainty	0.005 – 0.007	0.003 – 0.005	1%
Potential bias from fit algorithm (toy MC)	0.003 – 0.040	0.012 – 0.077	0 – 2.7%
Potential bias from fit ingredients (full MC)	0	0 – 0.017	0 – 7.1%
Incorrect CP assignment of decay	0.002 – 0.006	0.002 – 0.006	0
Effect of $K\pi$ S-wave contribution	0.005 – 0.023	0.006 – 0.014	5%
Peaking background mass shape	0 – 0.026	0 – 0.008	0 – 15.2%
Combinatorial background shapes vs $\cos\theta_{L,K}$	0.003 – 0.179	0.004 – 0.161	0 – 3.3%
Angular resolution	0 – 0.019	0	0
Signal mass shape	0	0	0.9%
Test of $\Gamma(B^0 \to K^{*0}J/\psi)/\Gamma(B^0 \to K^{*0}\psi')$	0	0	14.3%
Total systematic uncertainty	0.027 – 0.185	0.018 – 0.179	(15.5 – 21.5)%

For the branching ratio measurement, an additional normalization systematic uncertainty of 4.6% arises from the uncertainty on the branching fraction [13] of the normalization mode ($B^0 \to K^{*0}J/\psi$) . This uncertainty is not included in the results.

6 Results

The $K^+\pi^-\mu^+\mu^-$ invariant mass, $\cos\theta_K$, and $\cos\theta_l$ distributions for the q^2 bin corresponding to the $B^0 \to K^{*0}J/\psi$ decay are shown in Fig. 2, along with the projection of the maximum likelihood

fit described in Sec. 4. The results are used to validate the fit and obtain the values for F_S and A_S used in the fits to the signal q^2 bins. From 47 000 signal events, the longitudinal polarization fraction is measured to be $F_L = 0.554 \pm 0.004$(stat.), the dimuon forward-backward asymmetry is found to be $A_{FB} = -0.004 \pm 0.004$(stat.), the scalar fraction is $F_S = 0.01 \pm 0.01$(stat.), and the scalar-vector interference term is determined to be $A_S = -0.10 \pm 0.01$(stat.). The result for F_L is consistent with the world average value of 0.570 ± 0.008, while the value for A_{FB} is compatible with the expected result of no asymmetry. The same fit was performed for the $B^0 \to K^{*0}\psi'$ q^2 bin, where 3 200 signal events yielded results of $F_L = 0.509 \pm 0.016$(stat.), which is consistent with the world average value of 0.46 ± 0.04, and $A_{FB} = 0.013 \pm 0.014$(stat.), compatible with no asymmetry, as expected.

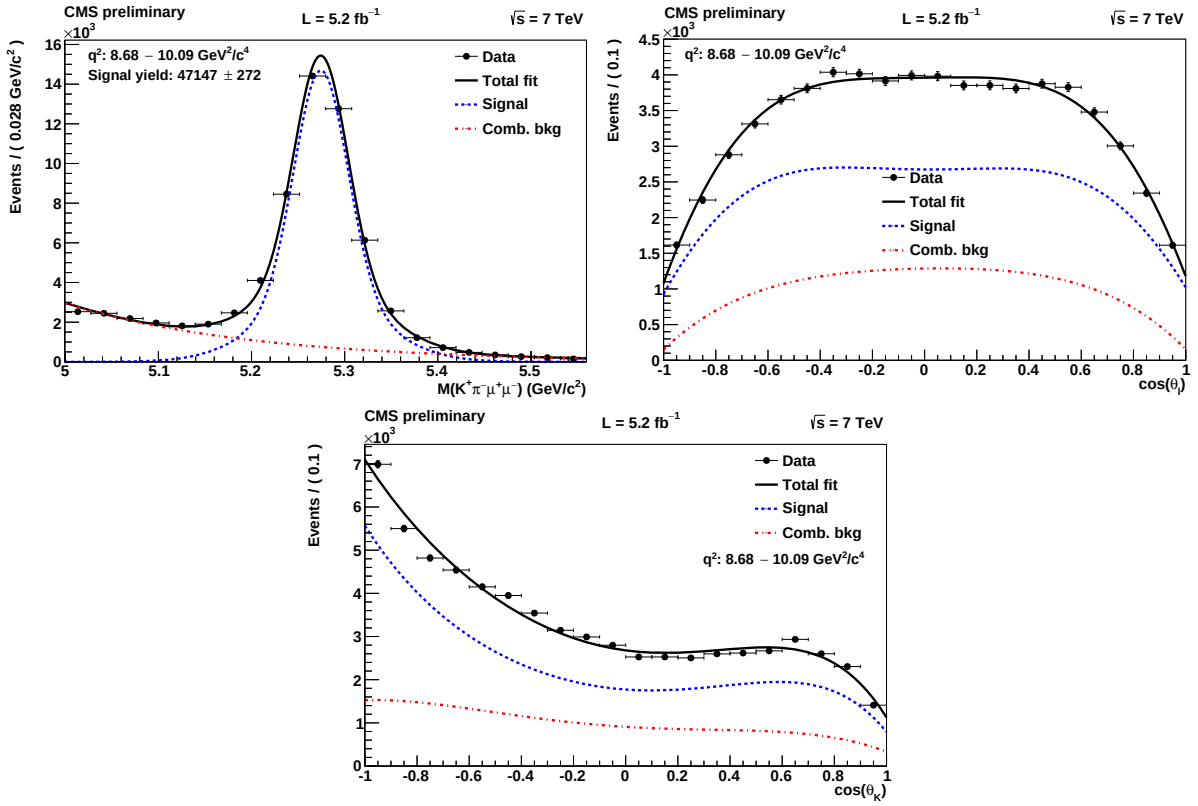

Figure 2: The $K^+\pi^-\mu^+\mu^-$ invariant mass (top left), $\cos\theta_l$ (top right), and $\cos\theta_K$ (bottom) distributions for the q^2 bin associated with $B^0 \to K^{*0}J/\psi$, along with projections of the unbinned maximum likelihood fit.

The $K^+\pi^-\mu^+\mu^-$ invariant mass distributions for each q^2 bin of the signal sample $B^0 \to K^{*0}$ $\mu^+\mu^-$ are shown in Fig. 3, along with the projection of the unbinned maximum likelihood fit described in Sec. 4. Clear signals are seen in each bin, with yields ranging from 23 ± 6 to 103 ± 12. From the fit, the K^{*0} longitudinal polarization fraction F_L and the forward-backward asymmetry of the muons A_{FB} are obtained in bins of q^2. These results are shown in Fig. 4, along with standard model predictions. The values of A_{FB} and F_L obtained for the first q^2 bin are at the physical boundary, which is enforced by a penalty term. This leads to statistical uncertainties, obtained from MINOS [14], of zero for the positive (negative) uncertainty for F_L (A_{FB}).

The standard model predictions are taken from Ref. [15], which is a combination of two theoretical techniques. In the low q^2 region a factorization approach [16] is used, which loses accuracy

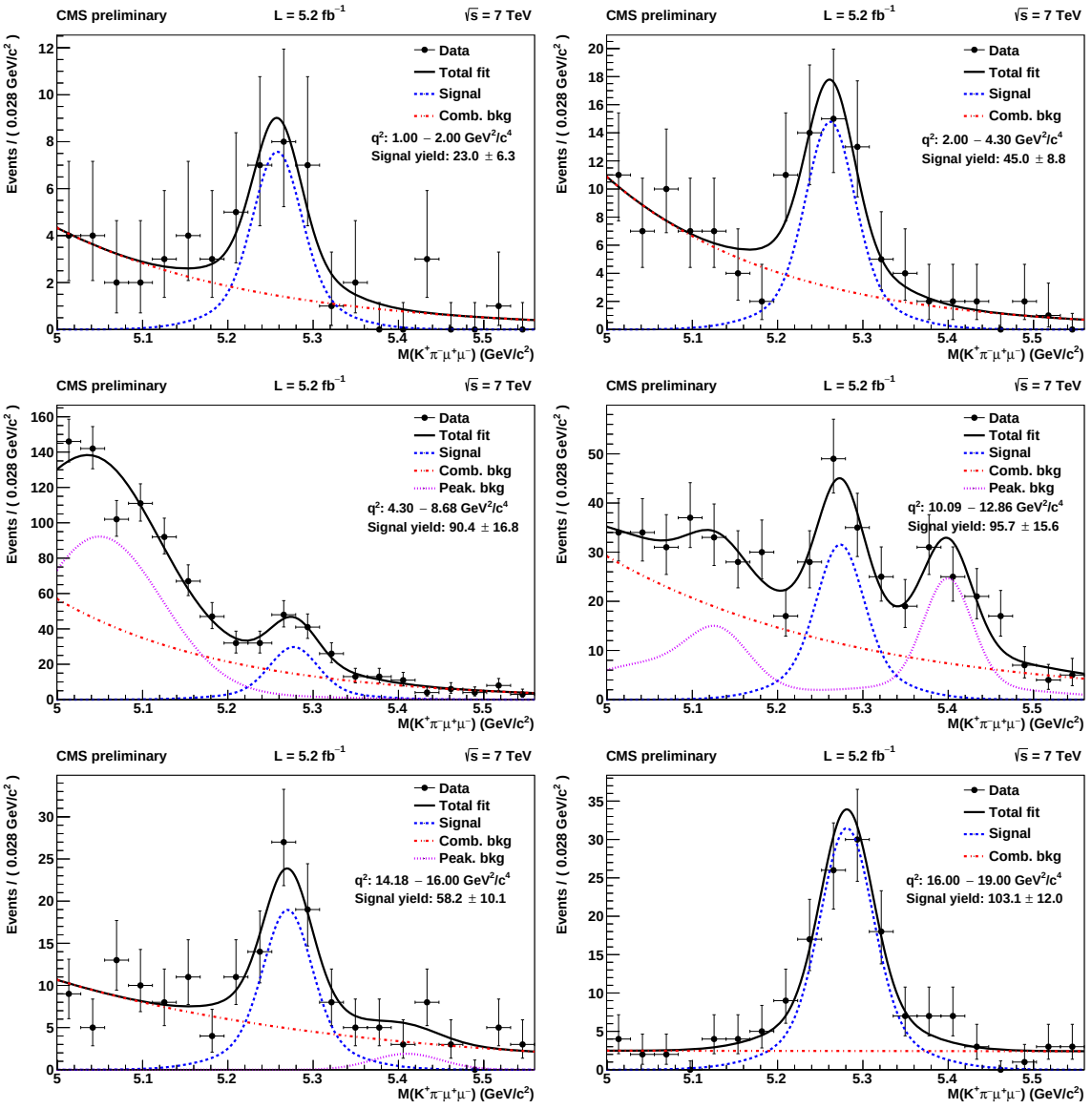

Figure 3: The $K^+\pi^-\mu^+\mu^-$ invariant mass distributions for each of the signal q^2 bins. Overlaid on each mass distribution is the projection of the unbinned maximum likelihood fit described in Sec. 4.

when approaching the J/ψ resonance. In the high q^2 region, an operator product expansion in the inverse b-quark mass, $1/m_b$, and in $1/\sqrt{q^2}$ is used [17], which is valid above the open charm threshold. In both regions, the form factor calculations are taken from Ref. [18] and a dimensional estimate is made on the uncertainty from expansion corrections [19].

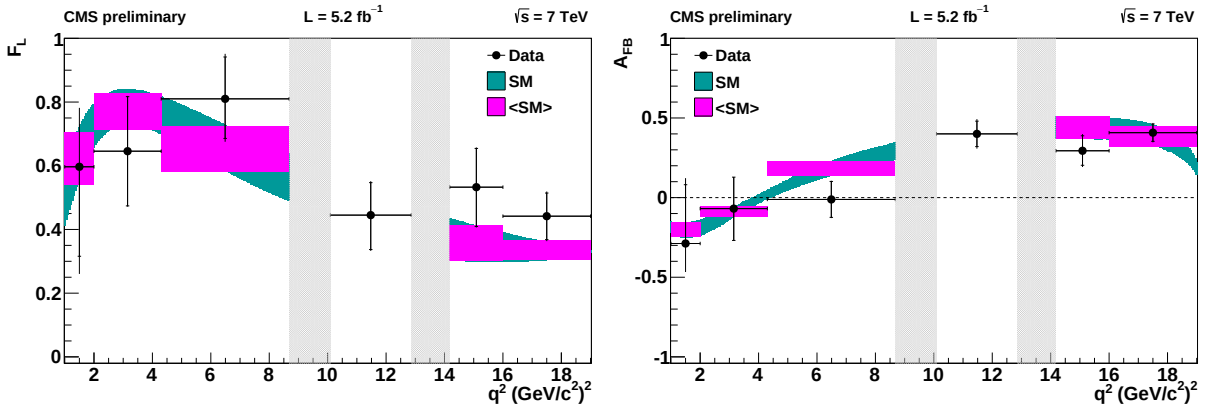

Figure 4: Results of the measurement of F_L (left) and A_{FB} (right) versus the dimuon q^2. The statistical uncertainty on the data points is shown by shorter error bars while the longer error bars give the total uncertainty. The gray shaded regions correspond to the J/ψ and ψ' resonances. The SM prediction is given by the cyan (light) band. The magenta (dark) regions are the result of rate-averaging the SM prediction across the q^2 bins to allow direct comparison to the data points.

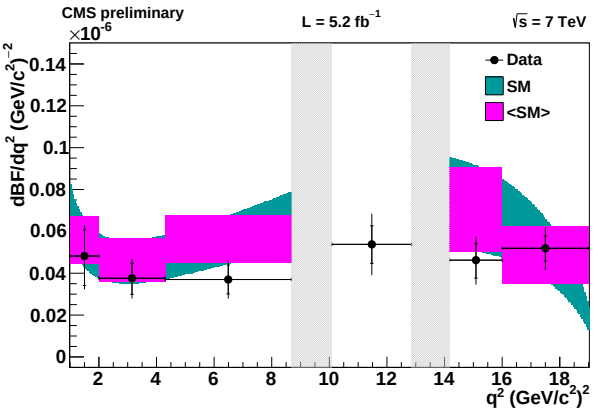

Figure 5: Results of the measurement of $d\mathcal{B}/dq^2$ versus the dimuon q^2. The statistical uncertainty on the data points is shown by shorter error bars while the longer error bars give the total uncertainty (not including the 4.6% normalization uncertainty). The gray shaded regions correspond to the J/ψ and ψ' resonances. The SM prediction is given by the cyan (light) band. The magenta (dark) regions are the result of rate-averaging the SM prediction across the q^2 bins to allow direct comparison to the data points.

Using the corrected yields for the signal and normalization mode ($B^0 \to K^{*0}\mu^+\mu^-$ and $B^0 \to K^{*0}J/\psi$) and the world average branching fraction for the normalization mode [13], the branching fraction for $B^0 \to K^{*0}\mu^+\mu^-$ is obtained as a function of q^2 and shown in Fig. 5, together with the SM predictions. The results for A_{FB}, F_L, and $d\mathcal{B}/dq^2$ are also reported in Table 2.

The angular observables can be theoretically predicted with good control of the relevant form factor uncertainties in the low dimuon invariant mass region. It is therefore interesting to

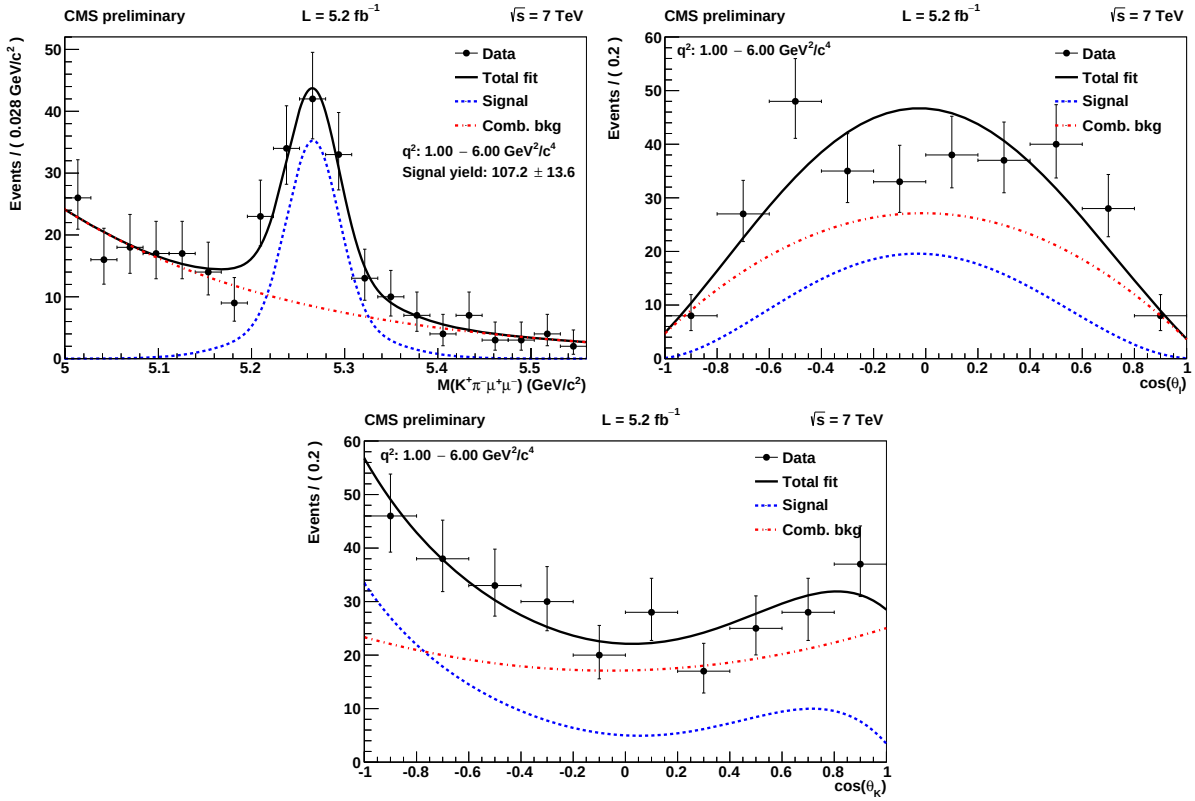

Figure 6: The $K^+\pi^-\mu^+\mu^-$ invariant mass (top left), $\cos\theta_l$ (top right), and $\cos\theta_K$ (bottom) distributions for $1 < q^2 < 6$ $(\mathrm{GeV}/c^2)^2$, along with projections of the unbinned maximum likelihood fit.

Table 2: Measurements of the fraction of longitudinal polarization of the $K^*(892)$ F_L, the forward-backward asymmetry of the muons A_{FB}, and the branching fraction of $B^0 \to K^{*0}\mu^+\mu^-$ in bins of q^2. The first uncertainty is statistical and the second is systematic. The branching fraction uncertainty does not include the 4.6% normalization uncertainty.

q^2 $(\mathrm{GeV}/c^2)^2$	F_L	A_{FB}	$\mathrm{d}\mathcal{B}/\mathrm{d}q^2$ $(10^{-8}\,c^4/\mathrm{GeV}^2)$
1 – 2	$0.60\,^{+0.00}_{-0.28} \pm 0.19$	$-0.29\,^{+0.37}_{-0.00} \pm 0.18$	$4.8\,^{+1.2}_{-1.4} \pm 0.8$
2 – 4.3	$0.65 \pm 0.17 \pm 0.03$	$-0.07 \pm 0.20 \pm 0.02$	$3.8 \pm 0.7 \pm 0.6$
4.3 – 8.68	$0.81\,^{+0.13}_{-0.12} \pm 0.05$	$-0.01 \pm 0.11 \pm 0.03$	$3.7 \pm 0.7 \pm 0.6$
10.09 – 12.86	$0.45\,^{+0.10}_{-0.11} \pm 0.03$	$+0.40 \pm 0.08 \pm 0.05$	$5.4 \pm 0.9 \pm 1.2$
14.18 – 16	$0.53 \pm 0.12 \pm 0.03$	$+0.29 \pm 0.09 \pm 0.05$	$4.6\,^{+0.8}_{-0.9} \pm 0.8$
16 – 19	$0.44 \pm 0.07 \pm 0.03$	$+0.41 \pm 0.05 \pm 0.03$	$5.2 \pm 0.6 \pm 0.8$

perform the measurements of the relevant observables in the $1 < q^2 < 6$ $(\mathrm{GeV}/c^2)^2$ region. The data results in this region, along with the fit projections, are shown in Fig. 6. The values obtained from this fit are: $F_L = 0.68 \pm 0.10(\mathrm{stat.}) \pm 0.02(\mathrm{syst.})$, $A_{FB} = -0.07 \pm 0.12(\mathrm{stat.}) \pm 0.01(\mathrm{syst.})$, and $\mathrm{d}\mathcal{B}/\mathrm{d}q^2 = (4.4 \pm 0.6(\mathrm{stat.}) \pm 0.7(\mathrm{syst.})) \times 10^{-8}\, c^4/\mathrm{GeV}^2$, where the systematic uncertainty on $\mathrm{d}\mathcal{B}/\mathrm{d}q^2$ does not include the 4.6% normalization uncertainty. These results are consistent with the SM predictions of $F_L = 0.74^{+0.06}_{-0.07}$, $A_{FB} = -0.04 \pm 0.03$, and $\mathrm{d}\mathcal{B}/\mathrm{d}q^2 = (4.9^{+1.0}_{-1.1}) \times 10^{-8}\, c^4/\mathrm{GeV}^2$ [20].

7 Summary

Using 5.2 fb^{-1} of data recorded with the CMS detector during 2011, an angular analysis of the decay $\mathrm{B}^0 \to \mathrm{K}^{*0}\mu^+\mu^-$ has been carried out. The data used for this analysis include more than 400 signal decays and 50 000 normalization/control mode decays ($\mathrm{B}^0 \to \mathrm{K}^{*0}\mathrm{J}/\psi$ and $\mathrm{B}^0 \to \mathrm{K}^{*0}\psi'$). Unbinned maximum likelihood fits were performed in bins of the dimuon invariant mass squared (q^2) with three independent variables: $\mathrm{K}^+\pi^-\mu^+\mu^-$ invariant mass, $\cos\theta_K$, and $\cos\theta_l$ to obtain values of the forward-backward asymmetry of the muons, A_{FB}, and the fraction of longitudinal polarization of the $\mathrm{K}^*(892)$, F_L. Using these results, unbinned maximum likelihood fits to the $\mathrm{K}^+\pi^-\mu^+\mu^-$ invariant mass in q^2 bins were used to extract the differential branching fraction $\mathrm{d}\mathcal{B}/\mathrm{d}q^2$. No deviations from the standard model predictions are found.

References

[1] F. Krüger et al., "Angular distribution and *CP* asymmetries in the decays $\bar{B} \to K^-\pi^+e^-e^+$ and $\bar{B} \to \pi^-\pi^+e^-e^+$", *Phys. Rev. D* **61** (2000) 114028, doi:10.1103/PhysRevD.61.114028,10.1103/PhysRevD.63.019901, arXiv:hep-ph/9907386.

[2] C. Bobeth, G. Hiller, and D. van Dyk, "The benefits of $\bar{B} \to \bar{K}^*l^+l^-$ decays at low recoil", *JHEP* **1007** (2010) 098, doi:10.1007/JHEP07(2010)098, arXiv:1006.5013.

[3] C. Bobeth et al., "The decay $\bar{B} \to \bar{K}\ell^+\ell^-$ at low hadronic recoil and model-independent $\Delta B = 1$ constraints", *JHEP* **1201** (2012) 107, doi:10.1007/JHEP01(2012)107, arXiv:1111.2558.

[4] BaBar Collaboration, "Angular distributions in the decay $B \to K^*l^+l^-$", *Phys. Rev. D* **79** (2009) 031102, doi:10.1103/PhysRevD.79.031102, arXiv:0804.4412.

[5] Belle Collaboration, "Measurement of the Differential Branching Fraction and Forward-Backword Asymmetry for $B \to K^{(*)}l^+l^-$", *Phys. Rev. Lett.* **103** (2009) 171801, doi:10.1103/PhysRevLett.103.171801, arXiv:0904.0770.

[6] CDF Collaboration, "Measurements of the Angular Distributions in the Decays $B \to K^{(*)}\mu^+\mu^-$ at CDF", *Phys. Rev. Lett.* **108** (2012) 081807, doi:10.1103/PhysRevLett.108.081807, arXiv:1108.0695.

[7] LHCb Collaboration, "Differential branching fraction and angular analysis of the decay $B^0 \to K^{*0}\mu^+\mu^-$", *Phys. Rev. Lett.* **108** (2012) 181806, doi:10.1103/PhysRevLett.108.181806, arXiv:1112.3515.

[8] CMS Collaboration, "CMS Absolute Calibration of the Luminosity Measurement at CMS: Winter 2012", CMS Physics Analysis Summary CMS-PAS-SMP 2012/008, (2012).

[9] CMS Collaboration, "The CMS experiment at the CERN LHC", *JINST* **3** (2008) S08004, doi:10.1088/1748-0221/3/08/S08004.

[10] T. Sjöstrand, S. Mrenna, and P. Skands, "PYTHIA 6.4 physics and manual", *JHEP* **0605** (2006) 026, doi:10.1088/1126-6708/2006/05/026, arXiv:hep-ph/0603175.

[11] D. Lange, "The EvtGen particle decay simulation package", *Nucl. Instrum. Meth. A* **462** (2001) 152, doi:10.1016/S0168-9002(01)00089-4.

[12] GEANT4 Collaboration, "GEANT4—a simulation toolkit", *Nucl. Instrum. Meth. A* **506** (2003) 250, doi:10.1016/S0168-9002(03)01368-8.

[13] Particle Data Group Collaboration, "Review of Particle Physics (RPP)", *Phys. Rev. D* **86** (2012) 010001, doi:10.1103/PhysRevD.86.010001.

[14] F. James and M. Roos, "Minuit – a system for function minimization and analysis of the parameter errors and correlations", *Comput. Phys. Commun.* **10** (1975) 343, doi:10.1016/0010-4655(75)90039-9.

[15] C. Bobeth, G. Hiller, and D. van Dyk, "General Analysis of $\bar{B} \to \bar{K}^{(*)}\ell^+\ell^-$ Decays at Low Recoil", *Phys. Rev. D* **87** (2012) 034016, doi:10.1103/PhysRevD.87.034016, arXiv:1212.2321.

[16] M. Beneke, Th. Feldmann, and D. Seidel, "Systematic approach to exclusive $B \to V\ell^+\ell^-, V\gamma$ decays", *Nucl. Phys. B* **612** (2001) 25, doi:10.1016/S0550-3213(01)00366-2, arXiv:hep-ph/0106067.

[17] B. Grinstein and D. Pirjol, "Exclusive rare $B \to K^*\ell^+\ell^-$ decays at low recoil: Controlling the long-distance effects", *Phys. Rev. D* **70** (2004) 114005, doi:10.1103/PhysRevD.70.114005, arXiv:hep-ph/0404250.

[18] P. Ball and R. Zwicky, "$B_{d,s} \to \rho, \omega, K^*, \phi$ decay form factors from light-cone sum rules reexamined", *Phys. Rev. D* **71** (2005) 014029, doi:10.1103/PhysRevD.71.014029, arXiv:hep-ph/0412079.

[19] U. Egede et al., "New observables in the decay mode $\bar{B}_d \to \bar{K}^{*0}\ell^+\ell^-$", *JHEP* **0811** (2008) 032, doi:10.1088/1126-6708/2008/11/032, arXiv:0807.2589.

[20] C. Bobeth, G. Hiller, and D. van Dyk, "More benefits of semileptonic rare B decays at low recoil: CP Violation", *JHEP* **1107** (2011) 067, doi:10.1007/JHEP07(2011)067, arXiv:1105.0376.